Light Harvesting and Charge Recombination in $CH_3NH_3PbI_3$ Perovskite Solar Cells Studied by Hole Transport Layer Thickness Variation

Nevena Marinova,[†,‡] Wolfgang Tress,[*,†] Robin Humphry-Baker,[†] M. Ibrahim Dar,[†] Vladimir Bojinov,[‡,§] Shaik Mohammed Zakeeruddin,[†] Mohammad Khaja Nazeeruddin,[†,Ψ] and Michael Grätzel[†]

[†]Laboratory of Photonics and Interfaces, Swiss Federal Institute of Technology (EPFL), Station 6, Lausanne, CH 1015, Switzerland, [‡]Department of Organic Synthesis, University of Chemical Technology and Metallurgy, 8 Kliment Ohridsky Str., 1756 Sofia, Bulgaria, and [§]Chemistry Department, Faculty of Sciences, [Ψ]Center of Excellence for Advanced Materials Research (CEAMR), King Abdulaziz University, P.O. Box 80203, Jeddah 21589, Saudi Arabia

ABSTRACT A tailored optimization of perovskite solar cells requires a detailed understanding of the processes limiting the device efficiency. Here, we study the role of the hole transport layer (HTL) spiro-MeOTAD and its thickness in a mesoscopic TiO_2-based solar cell architecture. We find that a sufficiently thick (200 nm) HTL not only increases the charge carrier collection efficiency but also the light harvesting efficiency. This is due to an enhanced reflection of a smooth HTL/Au—electrode interface. The rough $CH_3NH_3PbI_3$ perovskite surface requires an HTL thickness of >400 nm to avoid surface recombination and guarantee a high open-circuit voltage. Analyses of the electroluminescence efficiency and the diode ideality factor show that the open-circuit voltage becomes completely limited by trap-assisted recombination in the perovskite for a thick HTL. Thus, spiro-MeOTAD is a very good HTL choice from the device physics' point of view. The fill factor analyzed by the Suns-V_{oc} method is not transport limited, but trap-recombination limited as well. Consequently, a further optimization of the device has to focus on defects in the polycrystalline perovskite film.

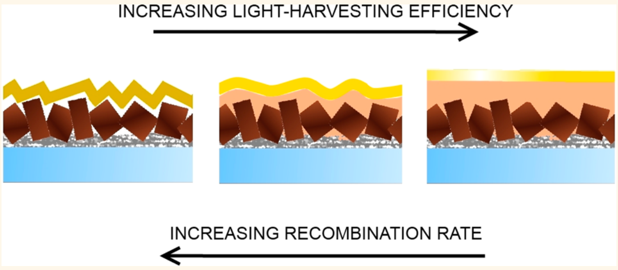

KEYWORDS: mesoscopic solar cell · spiro-MeOTAD · light-harvesting · electroluminescence · charge recombination · ideality factor

Methylammonium lead iodide perovskite ($MAPbI_3$) has drawn large attention over the last several years and is currently under intense investigation.[1−5] Since the first application of the perovskite in solar cells in 2009[6] with a power conversion efficiency (PCE) of 3.8%, the certified efficiency has recently reached 20.1%. The outstanding absorption properties, such as high absorption coefficient and suitable band gap, make this material very appropriate for light harvesting applications in photovoltaics.[7] Furthermore, $MAPbI_3$ is an ambipolar semiconductor, which can transport holes and electrons to their corresponding collector electrode. That is why $MAPbI_3$ perovskite solar cells (PSC) can operate even when no hole transport layer[8,9] or electron conductor[10,11] is used. The unique properties of the lead iodide perovskite combined with its low cost and easy processability make it promising for efficient and cheap third generation photovoltaic solar cells. Despite the inspiring results and impressive efficiency achieved, a deeper understanding of the fundamental working mechanisms of PSC becomes increasingly important. Better control of the light-harvesting and electronic properties of the PSC and identifying the role of the different components of the photovoltaic cells and their contribution to higher efficiency are still a challenge.

A standard mesoscopic perovskite solar cell comprises a fluorine-doped tin oxide (FTO)-coated glass, a TiO_2 layer as electron transport material and scaffold, a perovskite light absorbing layer, a hole-transporting layer (HTL), and a gold back electrode. The most commonly used hole transport material in PSCs is 2,2′7,7′-tetrakis(*N*,*N*-di-*p*-methoxyphenyl-amine)-9,9′-spirobifluoren (spiro-MeOTAD). Several desirable properties, e.g., a favorable glass transition temperature,

* Address correspondence to wolfgang.tress@epfl.ch.

Received for review January 21, 2015 and accepted February 27, 2015.

10.1021/acsnano.5b00447

solubility, ionization potential, and transparency in the visible spectral range make spiro-MeOTAD a suitable candidate for this application. The electronic properties of the material have been extensively investigated,[12,13] but the focus of those studies was mainly on the optimization of the performance by chemical p-doping of spiro-MeOTAD. The effect of different additives in the hole transport material composition has also been studied in details in refs 14−16.

Typically, the thicknesses of the different layers in PSC are in the range of tens to hundreds of nanometers. Thus, a change in the thickness or morphology of one of the layers affects the overall device performance. For example by varying the thickness of the perovskite, the absorption of the device can be tuned. A too thin layer (e.g., below 100 nm) results in low photocurrents due to insufficient absorption. Thicknesses above 500 nm usually result in a lower fill factor.[17,18] The size of the perovskite crystals also plays an important role. Im *et al.* show that a perovskite layer composed of crystals with size of 400−600 nm provides optimal light harvesting and charge extraction efficiency.[19] Similarly the thickness and porosity of the TiO_2 layer should be optimized in order to achieve maximal PCE.[20−22] However, in the literature there is little information about the influence of the HTL thickness on the device performance.

In this work we investigate the effect of spiro-MeOTAD thickness on the photovoltaic parameters in PSC. We analyze every parameter separately and relate the changes in photocurrent with the optical effects which we observe. Open-circuit voltage and charge recombination in the devices are investigated by means of electroluminescence. We apply the Suns-V_{oc} method[23] to obtain the series resistance of the devices, which affects the fill factor.

TABLE 1. Approximate HTL Thickness and Average Photovoltaic Parameters of the Devices Recorded under Standard AM1.5G Illumination (100 mW/cm^2) and Using an Aperture of 0.16 cm^2 on the Devices with an Active Area of ∼0.56 cm^2

device	HTL thickness [nm]	PCE [%]	J_{sc} [mA cm^{-2}]	V_{oc} [mV]	FF [%]
D0	0	5.9 ± 0.2	11.2 ± 0.6	689 ± 20	74 ± 2
D50	50	11.1 ± 1.2	16.8 ± 1.5	863 ± 35	75 ± 1
D100	100	12.7 ± 0.7	18.4 ± 0.9	915 ± 50	74 ± 2
D200	200	13.5 ± 0.4	18.6 ± 0.9	970 ± 21	74 ± 1
D400	400	13.1 ± 1.0	17.8 ± 1.0	992 ± 26	74 ± 3
D600	600	12.3 ± 1.2	17.6 ± 0.2	1004 ± 11	69 ± 5

RESULTS AND DISCUSSION

In our study we have fabricated PSC with different HTL thicknesses employing the sequential deposition method as reported by Burschka *et al.*[1] and further developed by Im *et al.*[19] The device comprises of FTO-coated glass on top of which a blocking layer of compact TiO_2 is deposited. A mesoporous TiO_2 structure is used as an electron transport material and as a scaffold for the perovskite absorber, the latter grows in the pores and additionally forms a capping layer on top of the TiO_2 surface. This capping layer is a polycrystalline structure, composed of perovskite grains. The HTL is then deposited by spin-coating of heavily doped (10 mol % FK209)[12] spiro-MeOTAD in chlorobenzene. To obtain different layer thicknesses the concentration of the solution as well as the spinning speed were varied (see Materials and Methods). The devices are completed by depositing a gold back electrode using thermal evaporation on top of the HTL or directly on the perovskite for the HTL free devices. We have prepared six types of devices with increasing HTL thickness, starting from 0 nm (D0) up to 600 nm (D600). Table 1 shows the approximate HTL thickness for the devices under investigation. SEM cross section images of a device without HTL and one with 400 nm HTL are depicted in Figure 1A and B, respectively. SEM images of all the devices under investigation are shown in SI. The perovskite capping layer consists of cuboids with size ∼200 nm which form a rough surface (Figure 1A). When the gold electrode is deposited directly on top of this surface, it follows the shape of the perovskite crystals and shows high roughness as well. When 400 nm HTL are deposited, a flat layer is formed on top of the perovskite, and the resulting back electrode is flat (Figure 1B).

Current density−voltage (*JV*) curves of the devices were recorded under standard illumination conditions of AM 1.5G (100 mW/cm^2) with a masking aperture of 0.16 cm^2 area. Figure 2 shows the solar cell metrics, i.e., PCE, open-circuit voltage (V_{oc}), short-circuit current

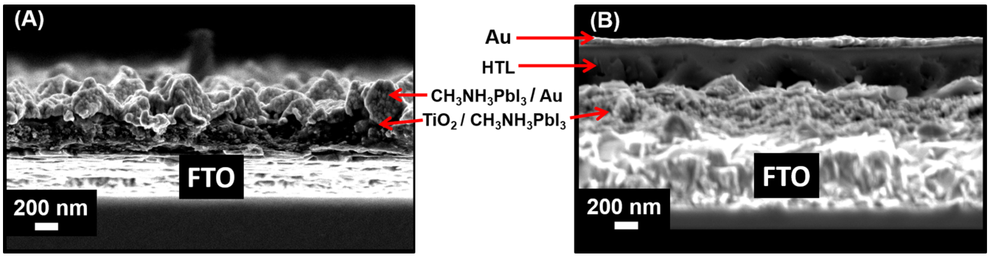

Figure 1. Cross sectional SEM images of (A) device D0 without hole-transport layer (HTL) and (B) device D400 with ∼400 nm thick HTL.

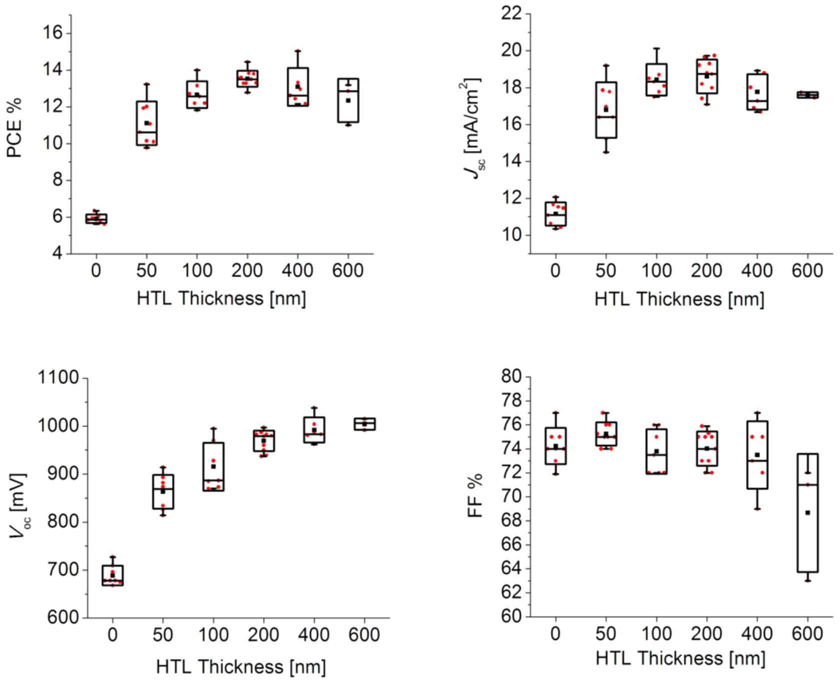

Figure 2. Effect of HTL thickness on PCE, J_{sc}, V_{oc}, and FF recorded at a light intensity of 1 Sun with masking aperture of 0.16 cm^2. Box represents the standard deviation, whiskers minimum and maximum values.

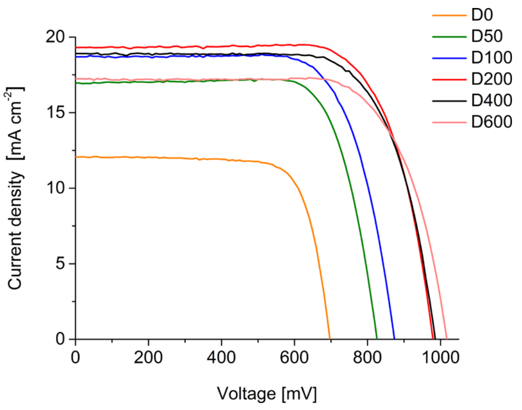

Figure 3. *JV* characteristics of devices with different HTL thickness from 0 to 600 nm measured under standard AM1.5G illumination.

density (J_{sc}), and fill factor (FF) as a function of HTL thickness. Apparently varying the HTL thickness affects all the photovoltaic parameters. As a result the average PCE shows an increase from 6.0% for D0 to a maximal value of 13.5% for D200 followed by a small drop to 13.1% for D400 and 12.3% for D600. *JV* curves of representative devices of each type are shown in Figure 3. It is worth mentioning that D0 shows a slight shunt, which is due to direct contact between the back gold electrode and TiO_2 in some regions as the gold penetrates deeply into the perovskite during the evaporation. Devices with HTL show no significant shunt in their *JV* curves when measured under 1 Sun illumination. Some of the devices show small hysteresis in the *JV* curve, which depends strongly on the scanning rate,[24] but does not affect the conclusions drawn here (Figure S7).

To get a better insight into the operation mechanism and the changes in the devices upon HTL thickness variation, we discuss each of the photovoltaic parameters separately.

Dependence of J_{sc} on HTL Thickness - Light Harvesting and Internal Quantum Efficiency. The short-circuit current density shows an increasing trend with thicker HTL, starting from 11.2 mA/cm^2 for D0 and reaching a maximum average value of 18.6 mA/cm^2 for D200. Further increasing the thickness does not dramatically change this parameter, suggesting that J_{sc} reaches saturation for HTL thicknesses between 200 and 400 nm. The difference in photocurrent for voltages below 600 mV does not significantly depend on voltage as obvious from the *JV* curves of Figure 3, and all devices have comparable FF. Consequently, either the voltage-independent part of the internal quantum efficiency (i.e., the ratio between extracted electrons to absorbed photons) is changed or the absorption of the perovskite is modified. To distinguish between these two possibilities, we recorded incident photon to current conversion efficiency (IPCE) of the devices and compared those to absorption measurements. The normalized IPCE spectra are shown in Figure 4A, where apparently the shapes of the spectra differ for the examined devices. This effect is pronounced in the spectral range between 500 and 750 nm. If we compare the spectra of D0 and D50, we see that the IPCE values in that region increase above average when an HTL is employed. A thicker HTL results in even higher

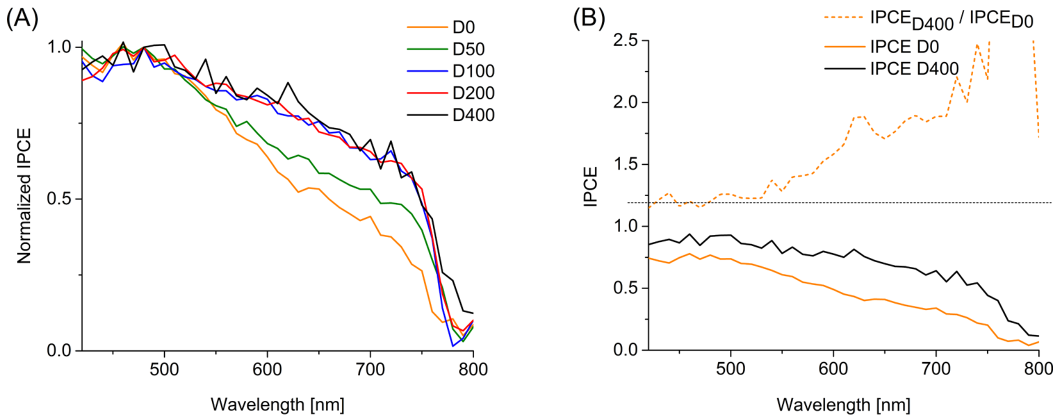

Figure 4. (A) Normalized IPCE spectra of the devices. (B) Absolute IPCE of device D0 and D400 (solid lines). The dashed line shows the ratio between IPCE of D400 and IPCE of D0.

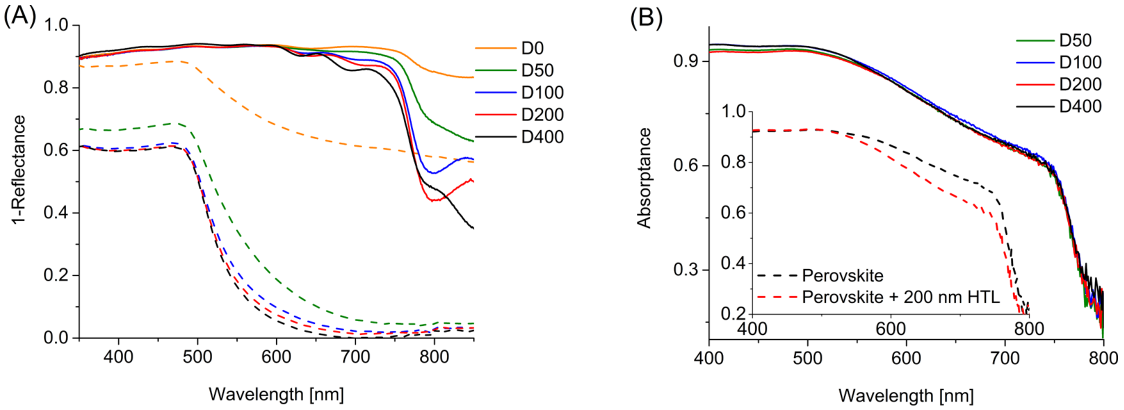

Figure 5. (A) Absorptance of the solar cells with gold electrode measured in reflection mode. Solid lines show the absorptance when illuminating through the glass, dashed lines when illuminating directly from the gold side. (B) Absorptance of the solar cell stacks without gold electrode measured with an integrating sphere. Inset shows the absorptance of D0 before and after deposition of 200 nm Spiro-MeOTAD.

IPCE values for these wavelengths. A further increase in the HTL thickness beyond 100 nm (D200 and D400) does not affect the IPCE, and the spectra of these devices match the spectrum of D100. Furthermore, we compare the absolute IPCE spectra for devices D0 and D400, shown in Figure 4B. The J_{sc} of the chosen devices is 18.9 mA/cm^2 for D400 and 12.1 mA/cm^2 for D0. The dashed line shows the ratio between both spectra, which is relatively constant for wavelengths smaller than 500 nm and increases with larger wavelengths. To understand this behavior, we perform several optical measurements.

We first measure the absorption of the complete cell containing the reflective back electrode. This can be easily done for our opaque solar cells, by measuring in reflection mode and applying the relation absorptance + transmittance + reflectance = 1. As the transmittance is <1% it is neglected in the analysis (Figure S8). The results are shown in Figure 5A. Solid lines represent the absorption of the device when illuminated through the glass substrate. Interestingly, the absorption in the spectral region above 600 nm is larger for the devices without HTL or very thin HTL despite the lower photocurrent recorded by the IPCE.

The dashed lines in Figure 5A show the absorption of the stack when illuminated from the gold side. They are mainly governed by the reflectivity of the gold electrode, which obviously differs significantly between the samples. For the devices with thick HTL D100, D200 and D400, the reflectivity is high for large wavelengths and the absorption sets in at 500 to 600 nm as expected for a yellowish gold mirror. However, the gold electrode for device D0 shows much higher absorption in the whole wavelength range, even for wavelengths larger than 800 nm, where none of the other materials in the stack significantly absorbs. This difference in the optical properties of the gold electrodes is so significant, that it can even be seen by eye (Figure 6). The electrode of devices without HTL looks darker and shows less specular reflection due to a high surface roughness (cf. Figure 1A). 50 nm thick HTL smooths the surface and the reflection improves, but not completely. Thicker HTL covers completely the rough perovskite crystals thus providing a flat surface and perfectly reflective gold electrode (Figure 1B). Consequently the higher absorption for D0 and D50 in the range above 750 nm when the devices are illuminated through the glass is due to increased absorption of the back electrode.

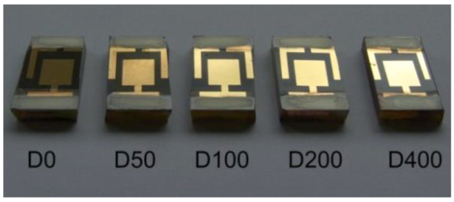

Figure 6. Photograph of the devices with increasing HTL thickness from left to right.

Next we record the absorption of the devices without the gold electrode, i.e., glass/FTO/TiO_2/perovskite/HTL films. The aim of this measurement is to estimate whether the perovskite absorption changes upon HTL deposition and if this change depends on the HTL thickness. For that purpose we remove carefully the gold electrode using sticky tape and place the device in an integrating sphere. The samples were successively positioned in the illumination beam and perpendicularly to the beam to compensate for secondary absorption. The results shown in Figure 5B reveal that the absorption of all the devices with HTL is practically the same, demonstrating that the HTL thickness does not influence the absorption of the perovskite. The spectra follow the absorption of the perovskite with large absorption coefficients for wavelengths smaller than 500 nm. For longer wavelengths, the absorption decreases gradually before dropping strongly between 750 and 800 nm, where the band edge of the perovskite is located. Note that the removal of the back electrode was not performed for D0, because it was not possible as the gold has penetrated deep in the perovskite and does not form a conformal layer (Figure 1). For that reason the absorption of D0 was measured separately (Figure 5B inset) on a fresh device without gold electrode. After the measurement 200 nm of HTL were deposited and the absorption was measured again. Apparently the perovskite absorption decreases after the deposition of HTL independent of HTL thickness. To check whether this decrease of absorption is due to a dissolution of the perovskite, a reference sample is investigated, where only a solvent mixture without spiro-MeOTAD was deposited. In that case the absorption does not change (Figure S9). Consequently, the decrease of absorption is caused by the spiro-MeOTAD layer itself, which increases transmission due to smoothing of the surface and slightly index matching with air (refractive index in the visible range is 2.2−2.4 for perovskite[25] and 1.8−2.0 for Spiro-MeOTAD[26]). Both effects reduce light trapping and reflection at the perovskite surface and thus absorption in the wavelength range where one light pass is not enough (550 to 800 nm).

If we consider the absorption of the devices with respect to the corresponding IPCE spectra, we observe inconsistent behavior in that D0 shows the lowest J_{sc} despite of exhibiting the highest light absorption. Devices with HTL show higher IPCE for wavelengths above 550 nm despite the lower absorption of the perovskite layer. The increase of current in this range for devices with HTL results from enhanced light harvesting efficiency thanks to the improved reflectivity of the gold electrode when a thick enough HTL is applied. For wavelengths larger than 550 nm, where one light pass through the perovskite layer is not sufficient to absorb all incoming light, the reflection of the gold electrode improves the light harvesting by a second light pass through the perovskite. The higher absorption observed when measuring from the glass side in D0 and D50 (Figure 5A, solid lines) is due to changes of the absorption in the gold electrode but photons absorbed in the gold cannot be converted into photocurrent. The lower reflectivity of the gold electrode does not increase the light absorption in the perovskite. In the yellow and red wavelength region, the absorption properties of the perovskite enhanced by the reflection of the gold back contact govern the IPCE of the devices. The IPCE monotonously decreasing with wavelength and not showing any interference patterns, confirms that this simple analysis is justified without considering interference effect and thin-film optics. The reason for this is that the devices show very rough interfaces giving rise to significant light scattering. In summary, this analysis demonstrates that the light harvesting efficiency can be enhanced by employing a thick enough HTL and decreases if the HTL is absent or too thin.

Coming back to the IPCE spectra of Figure 4B, we see that the ratio of the IPCE of D400 and D0 in the wavelength range between 400 and 550 nm is nearly constant. Here the absorptance of both devices is practically the same and is approaching 100%. Assuming that this wavelength-independent ratio of ca. 1.2 is also maintained for larger wavelengths, we estimate a difference in photocurrent between D0 and D400 of 2.4 mA/cm^2 (20%). This difference results from a change in the internal quantum efficiency, i.e. charge carrier collection efficiency, which is not expected to strongly depend on the wavelength. As the decrease of photocurrent for D0 compared to D400 is independent of voltage (cf. Figure 3), it indicates a loss of electrons or excited states by diffusion to the gold contact where they recombine with the holes. Uncovered perovskite surfaces might reduce the charge collection efficiency as well. However, this effect is supposed to be less relevant as the gold covers the perovskite capping layer without significantly large voids (Figure 1A) and the diffusion length of charge carriers in $MAPbI_3$ perovskite[27] are larger than the dimensions of possibly uncovered areas. The remaining 4.4 mA/cm^2 are then due to the increased absorption in the perovskite by light reflection from the Au overlayer.

To quantify the smoothing effect of the HTL we perform AFM measurements of the perovskite, HTL,

TABLE 2. Mean Roughness Values Measured by AFM

	mean roughness	
device	perovskite/HTL surface [nm]	gold surface [nm]
D0	88	50
D50	30	30
D100	22	14
D200	13	13
D400	13	6

and gold surface (images in SI). The mean roughness values for the devices are displayed in Table 2. With a value of 50 nm D0 shows the highest roughness of the gold electrode. This is due to the rough perovskite surface onto which the gold is deposited. The gold penetrates the perovskite layer during the evaporation process, and the back contact formed follows the profile of the rough perovskite layer (see also the SEM image in Figure 1). Applying a thin HTL smooths the perovskite, and the mean roughness of the gold surface drops to 30 nm for D50. Further increase of the HTL thickness results in better smoothing of the gold electrode, and the roughness of devices with 400 nm HTL is only 6 nm. A smooth HTL guarantees a conformal contact with the thin evaporated back electrode thus contributing to optimization of the photocurrent of the devices.

Dependence of V_{oc} on HTL Thickness - Influence on Recombination. The average V_{oc} for the HTL free devices is around 690 mV, which is a very low value for common PSC. Employing an HTL improves V_{oc}, which gradually increases as the HTL thickness increases reaching values above 1 V for device D600 (Figure 2). The open-circuit voltage in a solar cell with a given absorber depends mainly on the recombination in the device. Consequently, every factor that affects recombination will also affect V_{oc}. To have a more realistic idea about the changes of V_{oc} in the devices, we remeasure this parameter under 1 Sun illumination conditions without masking aperture. Thus, the recorded value for V_{oc} comes from the same area as the dark current, i.e., the whole device area. The real V_{oc} values are listed in Table 3. As expected they are higher than the values measured with masking aperture, but the trend remains the same: V_{oc} decrease as HTL thickness decreases. The loss of the V_{oc} for HTL free devices and those with thin HTL is due to higher recombination rates. To prove this, we performed electroluminescence measurements, where current is being injected into the PSC and the electroluminescence (EL) intensity of the device is recorded as a function of the injection current. The electroluminescence quantum yield EQE_{EL} can be calculated by dividing the emitted photon flux by the injected electron current. The EL radiation is a result of electron–hole recombination in the perovskite and reflects

TABLE 3. Measured and Calculated Values for V_{oc}[a]

			Nonradiative loss [V]		V_{oc} calc [V]	
device	V_{oc} [V]	EQE_{EL}	300 K	320 K	300 K	320 K
D0	0.80	3×10^{-9}	0.51	0.54	0.82	0.79
D50	0.87	2.6×10^{-8}	0.45	0.48	0.88	0.85
D100	0.96	8.5×10^{-7}	0.36	0.39	0.97	0.94
D200	0.98	1.6×10^{-6}	0.34	0.37	0.99	0.96
D400	1.00	3.1×10^{-6}	0.33	0.35	1.00	0.98
D600	1.05	5×10^{-5}	0.26	0.27	1.07	1.06

[a] The value for the EQE_{EL} is determined at a driving current that equals the photocurrent under 1 Sun illumination.

the radiative recombination process in the device. In our previous work we have predicted a theoretical limit for the open-circuit voltage $V_{oc,rad}$ of 1.33 V for $MAPbI_3$ perovskite solar cells, which is given only by the perovskite material and not by the device architecture.[28] This number represents the V_{oc} in an ideal case when recombination in the device is only radiative, which corresponds to $EQE_{EL} = 1$. In reality the V_{oc} is lower due to additional nonradiative recombination. Knowing the EQE_{EL} allows us to theoretically predict the real open-circuit voltage and estimate the fraction of nonradiative recombination in the cell. The relation between V_{oc} and EQE_{EL} is given by

$$V_{oc,\,calc} = V_{oc,\,rad} - \frac{k_B T}{e} \ln(1/EQE_{EL}) \qquad (1)$$

where $V_{oc,rad}$ is the theoretical (i.e., radiative) limit of V_{oc} for perovskite, which comes to 1.33 V[28] (for 1 Sun illumination and T = 300 K), k_B is the Boltzmann constant, T the temperature, and e the elementary charge. We perform the calculation for two temperatures 300 and 320 K, which gives us the temperature range at which our devices are supposed to operate. The results are shown in Table 3.

The quantum efficiency of radiative recombination is strongly affected by the thickness of the HTL implying that this impacts also the share of radiative and nonradiative recombination. Devices with thick HTL show higher EQE_{EL} and V_{oc}. Decreasing the thickness of HTL results in lower EQE_{EL} as the fraction of nonradiative loss rises due to recombination at the exposed gold contact ("surface recombination").[29]

In Figure 7 the EQE_{EL} of the devices with different HTL thickness is plotted as a function of the injection current (J_{inj}). The EQE_{EL} increases substantially with the injection current, meaning that radiative recombination becomes more likely for larger currents. That is intuitively expected as charge carrier densities increase with driving voltage favoring direct recombination between electrons in the conduction band and holes in the valence band compared to trap mediated recombination.[28]

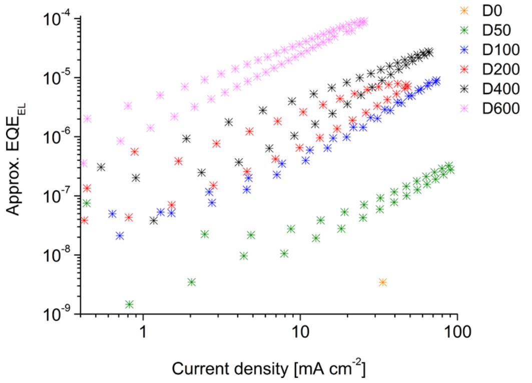

Figure 7. EQE_{EL} as a function of the injection current. The measurement was performed scanning from low to high forward bias voltage and back. The difference between the scan directions is an indication for the accuracy of the measurement due to reversible instabilities of the devices. The spreading is also similar to the range of device-to-device variations.

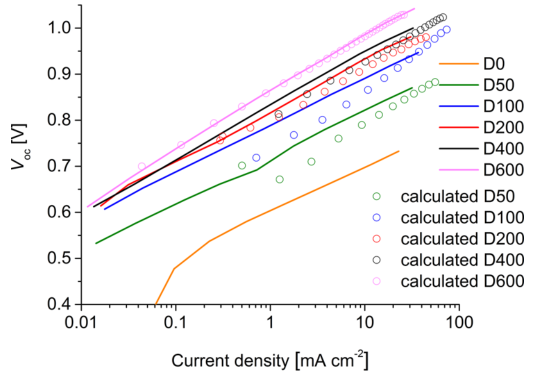

Figure 8. Calculated and measured V_{oc} as a function of the injection and short-circuit current density, respectively. The short-circuit current density is proportional to the light intensity (Figure S15).

Based on these data, V_{oc} can be predicted for different light intensities. To calculate V_{oc}, we again use eq 1, but take into account that $V_{oc,rad}$ depends on the light intensity via the photocurrent J_{ph}:

$$V_{oc,\,calc} = \frac{k_B T}{e} \ln\left(\frac{J_{ph}}{J_{em,\,0}}\right) - \frac{k_B T}{e} \ln\left(\frac{1}{EQE_{EL}(J_{inj})}\right) \qquad (2)$$

Here, $J_{em,0}$ is the emission current when the device is in equilibrium with the ambient blackbody radiation.[28] As J_{ph} increases linearly with the light intensity in the investigated range (Figure S15), we can use J_{ph} as a direct measure of the light intensity, which allows us to compare the measured V_{oc} with the one predicted from the EQE_{EL} at a certain injection current $J_{inj} = J_{ph}$.

The solid lines in Figure 8 show V_{oc} measured at several light intensities in the range 0.001−2 Suns and plotted as a function of J_{ph}, where 1 Sun equals a J_{ph} between 10 and 20 mA/cm^2 dependent on the device (cf. Table 1). The V_{oc} of all devices increases logarithmically with light intensity, where both the overall value and the slope increase with HTL thickness. The exceptional drop of V_{oc} for D0 at low intensity (photocurrents <0.5 mA/cm^2) is due to a significant shunt in this device. The calculated V_{oc} as a function of the injection current is depicted with circles in the graph. The theoretical and experimental data show the same trend, and the calculated values closely match the measured V_{oc}. These results clearly show that eq 2 can be applied for predicting the V_{oc} of PSC for different light intensities.

Investigating the slope of V_{oc} as a function of light intensity provides insights into the dominating recombination mechanism. We observe that the slope increases from 96 to 125 mV/decade from device D0 to D600. These values are in agreement with reported data.[30] The slope of D600 comes very close to the theoretically expected slope of 120 mV/decade for the case of purely trap-assisted recombination (Shockley−Read−Hall, SRH). This is in accordance with the observation of a first-order recombination mechanism dominating solar cell performance at charge carrier densities expected for illumination intensity ≤ several Suns.[31,32] The reduced (and less constant) slope for devices with thinner HTL is attributed to surface recombination at the hole collecting contact. Thus, additional recombination at the hole contact is responsible for both the overall reduction of V_{oc} and the reduction of the slope of V_{oc} as a function of light intensity. The reason for these superimposing phenomena is the mesoscopic nature of the device with significant spatial inhomogeneities and nonplanarity of surfaces paired with large diffusion lengths of charge carriers, resulting in a three-dimensional extension of the hole-collecting contact.

We can relate the intensity dependence of V_{oc} to the diode ideality factor n, which is originally defined for the current−voltage relation of a diode following the Shockley equation:

$$J = J_0(e^{eV/nk_BT} - 1) - J_{ph} \qquad (3a)$$

Setting J to 0 yields with $J_{ph} \gg J_0$:

$$V_{oc} = \frac{nk_BT}{e} \ln\left(\frac{J_{ph}}{J_0}\right) \qquad (3b)$$

The physical reason for introducing the ideality factor is to account for additional recombination in the space charge region of a diode. Eq 3a without J_{ph} and an ideality factor of 1 describes a diffusion-dominated diode current in the dark implying only direct recombination between electrons and holes, whereas an n of 2 signifies purely SRH type of recombination. Comparing eqs 2 and 3b, we see that an n of 1 requires an EQE_{EL} which is independent of driving current, whereas higher values of n are represented by an EQE_{EL} that increases with current, peaking at a linear increase of EQE_{EL} with driving current, adding another k_BT/e to the slope of V_{oc} as a function of light intensity. Using eq 3b, we translate the slopes into

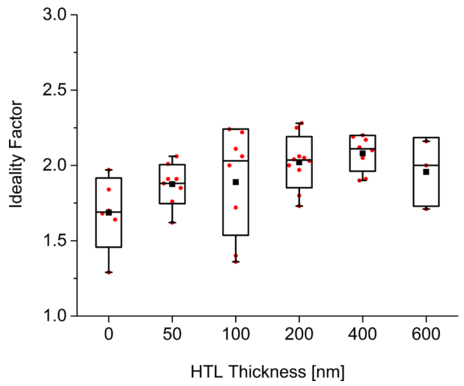

Figure 9. Diode ideality factor as a function of HTL thickness. Boxes represent the standard deviation, whiskers minimum and maximum value. The values were calculated from the differential slope of the semilogarithmic dark *JV* curves similar to the procedure in ref 33, where the plateau value in the range between 0.6 and 0.9 V was taken (Figure S16).

ideality factors of 1.6 (D0) to 2.1 (D600). According to eq 3a, *n* can also be determined from the *JV* curve measured in the dark. The results ranging from 1.7 to 2.1 are shown in Figure 9, which reproduce the trends from the analysis under illumination.

Dependence of the FF on the HTL Thickness - Recombination and Series Resistance Losses. To investigate the effect of recombination on the fill factor and separate it from charge extraction limitations, we perform an analysis oriented at the Suns-V_{oc} method.[23] This is a widely used characterization method for different types of solar cells,[34] in particular to accurately investigate the influence of the series resistance on the fill factor. The method consists of measuring the V_{oc} ($V_{\text{Suns-}V_{oc}}$) of the device at different light intensities. The recorded V_{oc} values are used to determine pseudo-*JV* curves, which only reflect generation and recombination processes without the effect of the series resistance as no current is flowing during the measurement of $V_{\text{Suns-}V_{oc}}$. To obtain the pseudo-*JV* curve, the light intensity (I) is associated with implied current density:

$$J = \frac{I - I(1\,\text{Sun})}{I(1\,\text{Sun})} J_{\text{sc}(1\,\text{Sun})} \tag{4}$$

Figure 10 shows the pseudo and measured *JV* curves at different light intensities for device D200. The graphical comparison reveals that they completely coincide for 0.25 suns and show very small difference for 1 Sun. Consequently, the fill factor of the real *JV* curve is only slightly limited by a series resistance and approaches its maximum given by the recombination. This value is ∼82% and can only be improved if the SRH recombination is reduced. Thus, the performance is not limited by transport of charges in the perovskite or in any other layer such as TiO_2 or HTL.

The value of the series resistance R_s can be calculated considering the voltage loss between the two *JV* curves at a given *J*:

$$R_s = \frac{V_{JV}(J) - V_{\text{Suns-}V_{oc}}(J)}{J} \tag{5}$$

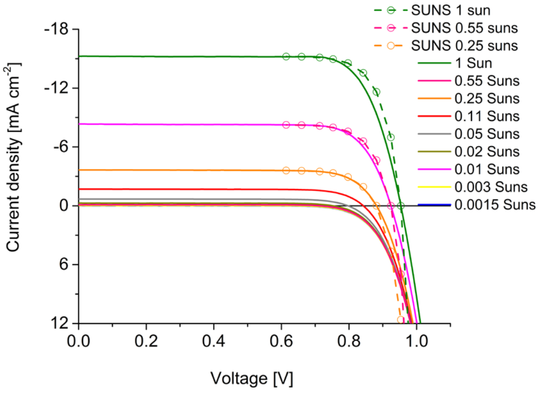

Figure 10. Measured *JV* curves (solid) and pseudo *JV* curves deduced from the Suns-V_{oc} method (dashed) for device D200 at different light intensities.

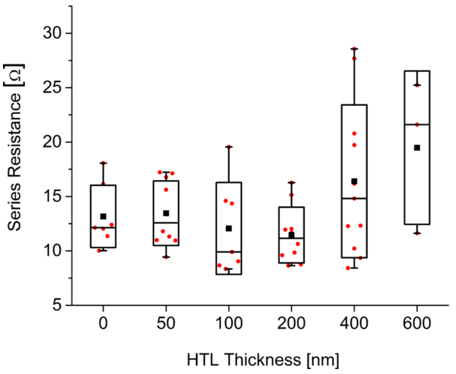

Figure 11. Series resistance as a function of HTL thickness, extracted from the slope of the dark *JV* curves between 1.4 and 1.6 V. Boxes represent the standard deviation, whiskers min and max value. The series resistance is determined for a device area of 0.56 cm^2 and includes the sheet resistance of the electrodes dominating lateral charge transport.

Investigating all devices at voltages close to V_{oc}, we obtain values for R_s between 12 and 20 Ω, which are almost independent of voltage (Figure S17).

The series resistance can also be approximately deduced from the *JV* curves measured in the dark and compared to the fill factor as a function of the HTL thickness. Figure 2 shows that the FF of the devices under investigation remains constant at around 74% for HTL thickness 0–400 nm. For thicker HTL it drops slightly reaching 69%. Possible reason for this effect is the increased series resistance R_s when the thickness of the HTL increases. To prove this statement we calculate the series resistance of all the devices from the dark *JV* curves. We extract the R_s from the slope of the curves between 1.4 and 1.6 V and plot it in Figure 11. The R_s is between 10 and 15 Ω for D0–D200, rises slightly to 17 Ω in D400 and reaches 20 Ω in D600. We have estimated that roughly 5 Ω originate from the sheet resistance of the FTO. Consequently, the conductivity of the HTL does not limit the FF for layer thicknesses in the 100s of nm range. This is due to the high doping concentration of the spiro-MeOTAD, which explains the differences to results presented in ref 14.

CONCLUSIONS

The perovskite solar cell is a nanoscale device and the thickness of the HTL affects the performance and the photovoltaic parameters. A sufficiently thick (200 nm) HTL not only increases the charge carrier collection efficiency but also the light harvesting efficiency due to an enhanced reflection from the smooth HTL/Au−electrode interface. This effect can be crucial for enhancing light harvesting efficiency and obtaining high photocurrents because the perovskite absorption of devices with optimized layer thicknesses is not sufficient for light with wavelength >500 nm. The rough perovskite surface requires an HTL thickness of >400 nm to avoid surface recombination and guarantee a high open-circuit voltage. Analyses of the electroluminescence efficiency and the diode ideality factor show that the open-circuit voltage becomes completely limited by trap-assisted recombination in the perovskite for thick HTL. Thus, spiro-MeOTAD is a very good HTL choice from the device physics' point of view. The fill factor analyzed by the Suns-V_{oc} method is not transport limited, but trap-recombination limited as well. Consequently, a further optimization of the device has to focus on defects in the polycrystalline perovskite film. These results contribute to a better understanding of the limiting processes in perovskite-based solar cells.

MATERIALS AND METHODS

Photovoltaic Characterization. Current−voltage characteristics were recorded by applying an external potential bias to the cells while recording the generated photocurrent with a digital source meter (Keithley Model 2400). The light source was a 450 W xenon lamp (Oriel) equipped with a Schott K113 Tempax sunlight filter (Praezisions Glas and Optik GmbH) to match the emission spectrum of the lamp to the AM1.5G standard. Before each measurement, the exact light intensity was determined using a calibrated Si reference diode equipped with a color matching filter (KG-3, Schott). The voltage step was 10 mV, settling time was 100 ms, and integration time was 100 ms.

IPCE Spectra. The spectra were recorded as functions of wavelength under a constant white light bias of ∼5 mW cm^{-2} supplied by an array of white light-emitting diodes. The excitation beam coming from a 300 W xenon lamp (ILC Technology) was focused through a Gemini-180 double monochromator (Jobin Yvon Ltd.) and chopped at ∼2 Hz. The signal was recorded using a Model SR830 DSP Lock-In Amplifier (Stanford Research Systems). Unless stated elsewhere, all measurements were conducted using a nonreflective metal aperture of 0.16 cm^2.

EL. The EQE_{EL} was detected measuring the emitted photon flux with a large-area Si-photodetector positioned close to the sample. Due to the nonconsidered angular dependence of emission and detector sensitivity, the EQE_{EL} is expected to be underestimated by a factor between 1 and 2. The driving voltage was applied using a Bio-Logic SP300 potentiostat, which was also used to measure the short-circuit current of the detector.

Reflection Measurements. The reflection measurements were carried out on Varian Cary 5 spectrophotometer, using an integrating sphere of 110 mm diameter. The samples were placed over the reflection port on the backside of the sphere and the total reflection (specular and diffused) of the sample was measured.

Absorption Measurements. The absorption measurements were done in a 102 mm diameter integration sphere (Horiba F-3018) in a Fluorolog 322 (Horiba Jobin Yvon Ltd. Spectrofluorometer). Samples were illuminated with a 450 W Xe lamp filtered through a double monochromator (slit width 1 mm) directed into the sphere. The samples were measured successively at 90° and 0° from the incoming beam, and the spectra were subtracted to correct for scattering. The outgoing beam was filtered through a 0.5% gray filter (Horiba). All the spectra were photometrically corrected. The emission monochromator was scanned synchronously with the excitation monochromator.

Atomic Force Microscopy. The AFM measurements were performed on multimode (Bruker Nano Surface, Santa Barbare, CA) in tapping mode.

SEM cross sections. A field-emission scanning electron microscope (FESEM, Merlin and Leo 1525) was employed to analyze the morphology of the samples. An electron beam accelerated to 3 kV was used with an in-lens detector.

Device Fabrication. Devices were prepared on clean FTO-coated glass (NSG 10). A blocking layer of compact TiO_2 was deposited by spray pyrolysis of precursor solution of 0.6 mL titanium diisopropoxidebis(acetylacetonate) in 9 mL ethanol and 0.4 mL of acetylacetone, with oxygen as carrier gas at 450 °C. The mesoporous TiO_2 was formed by spin coating of colloidal solution of TiO_2 with particle size of 20 and at 5000 rpm for 20 s. The films were then gradually heated to 500 °C and sintered at that temperature for 15 min. One M lead iodide DMF solution was spin coated onto the mesoporous TiO_2 at 6500 rpm for 30 s and dried at 70 °C. After drying, the deposition of lead iodide was repeated in order to ensure a better loading of the mesoporous structure with lead iodide. The perovskite layer was formed after drop-casting 0.2 mL CH_3NH_3I solution in isopropanol (8 mg mL^{-1}) onto the substrates and after waiting for 20 s was then spin-coated for 20 s at 4000 rpm. The substrates were then dried at 70 °C. For the devices D100, D200, and D400, a solution of 72.3 mg (0.06M) spiro-MeOTAD in 1 mL chlorobenzene was prepared, containing 10 mol % FK 209, 28.8 μL (350% molar ratio to spiro-MeOTAD) *tert*-butylpyridine, and 17.5 μL (50% molar ratio to spiro-MeOTAD) solution of lithium bis(trifluoromethylsulfonyl)imide (Li-TFSI 520 mg/mL in acetonitrile). The HTL solution was spin coated onto the perovskite surface for 20 s, and the spinning speed was varied as follows: D100, 4000 rpm; D200, 2000 rpm; and D400, 700 rpm. For D50 the spiro OMeTAD concentration was decreased by half, while the ratio of additives remained the same. The solution was spin-coated at 4000 rpm for 20 s. Analogously, the spiro-MeOTAD concentration was increased by 1.5 for D600, the ratio of the additives remained the same, and the solution was spin-coated at 700 rpm for 20 s. The device architecture was completed with an 80 nm gold counter electrode, which was thermally evaporated on top of the device. The active area of the devices was ∼0.56 cm^2.

Conflict of Interest: The authors declare no competing financial interest.

Supporting Information Available: Cross sectional SEM images, hysteresis measurement, transmission measurements, AFM images of the gold electrode, J_{sc} as a function of light intensity, ideality factor, and series resistance. This material is available free of charge via the Internet at http://pubs.acs.org.

Acknowledgment. N.M. and S.M.Z. acknowledge Sciex fellowship under Project Code: 12.249. W.T. and M.K.N. thank the European Union for funding within the Seventh Framework Program [FP7/2007-2013] under grant agreement no. 604032 of the MESO project.

REFERENCES AND NOTES

1. Burschka, J.; Pellet, N.; Moon, S.-J.; Humphry-Baker, R.; Gao, P.; Nazeeruddin, M. K.; Grätzel, M. Sequential Deposition as a Route to High-Performance Perovskite-Sensitized Solar Cells. *Nature* **2013**, *499*, 316–319.
2. Liu, M.; Johnston, M. B.; Snaith, H. J. Efficient Planar Heterojunction Perovskite Solar Cells by Vapour Deposition. *Nature* **2013**, *501*, 395–398.
3. Jeon, N. J.; Noh, J. H.; Kim, Y. C.; Yang, W. S.; Ryu, S.; Seok, S., Il. Solvent Engineering for High-Performance Inorganic-Organic Hybrid Perovskite Solar Cells. *Nat. Mater.* **2014**, *13*, 897–903.
4. Zhou, H.; Chen, Q.; Li, G.; Luo, S.; Song, T. -b.; Duan, H.-S.; Hong, Z.; You, J.; Liu, Y.; Yang, Y. Interface Engineering of Highly Efficient Perovskite Solar Cells. *Science* **2014**, *345*, 542–546.
5. Dou, L.; Yang, Y. M.; You, J.; Hong, Z.; Chang, W.-H.; Li, G.; Yang, Y. Solution-Processed Hybrid Perovskite Photodetectors with High Detectivity. *Nat. Commun.* **2014**, *5*, 5404.
6. Kojima, A.; Teshima, K.; Shirai, Y.; Miyasaka, T. Organometal Halide Perovskites as Visible-Light Sensitizers for Photovoltaic Cells. *J. Am. Chem. Soc.* **2009**, *131*, 6050–6051.
7. Im, J.-H.; Lee, C.-R.; Lee, J.-W.; Park, S.-W.; Park, N.-G. 6.5% Efficient Perovskite Quantum-Dot-Sensitized Solar Cell. *Nanoscale* **2011**, *3*, 4088–4093.
8. Etgar, L.; Gao, P.; Xue, Z.; Peng, Q.; Chandiran, A. K.; Liu, B.; Nazeeruddin, M. K.; Grätzel, M. Mesoscopic $CH_3NH_3PbI_3$/TiO_2 Heterojunction Solar Cells. *J. Am. Chem. Soc.* **2012**, *134*, 17396–17399.
9. Mei, A.; Li, X.; Liu, L.; Ku, Z.; Liu, T.; Rong, Y.; Xu, M.; Hu, M.; Chen, J.; Yang, Y.; et al. A Hole-Conductor−free, Fully Printable Mesoscopic Perovskite Solar Cell with High Stability. *Science* **2014**, *345*, 295–298.
10. Lee, M. M.; Teuscher, J.; Miyasaka, T.; Murakami, T. N.; Snaith, H. J. Efficient Hybrid Solar Cells Based on Meso-Superstructured Organometal Halide Perovskites. *Science* **2012**, *338*, 643–647.
11. Liu, D.; Yang, J.; Kelly, T. L. Compact Layer Free Perovskite Solar Cells with 13.5% Efficiency. *J. Am. Chem. Soc.* **2014**, *136*, 17116–17122.
12. Burschka, J.; Kessler, F.; Nazeeruddin, M. K.; Grätzel, M. Co(III) Complexes as P-Dopants in Solid-State Dye-Sensitized Solar Cells. *Chem. Mater.* **2013**, *25*, 2986–2990.
13. Fantacci, S.; De Angelis, F.; Nazeeruddin, M. K.; Grätzel, M. Electronic and Optical Properties of the Spiro-MeOTAD Hole Conductor in Its Neutral and Oxidized Forms: A DFT/TDDFT Investigation. *J. Phys. Chem. C* **2011**, *115*, 23126–23133.
14. Dualeh, A.; Moehl, T.; Tétreault, N.; Teuscher, J.; Gao, P.; Nazeeruddin, M. K.; Grätzel, M. Impedance Spectroscopic Analysis of Lead Iodide Perovskite-Sensitized Solid-State Solar Cells. *ACS Nano* **2014**, *8*, 362–373.
15. Abate, A.; Leijtens, T.; Pathak, S.; Teuscher, J.; Avolio, R.; Errico, M. E.; Kirkpatrik, J.; Ball, J. M.; Docampo, P.; McPherson, I.; et al. Lithium Salts as "Redox Active" p-Type Dopants for Organic Semiconductors and Their Impact in Solid-State Dye-Sensitized Solar Cells. *Phys. Chem. Chem. Phys.* **2013**, *15*, 2572–2579.
16. Noh, J. H.; Jeon, N. J.; Choi, Y. C.; Nazeeruddin, M. K.; Grätzel, M.; Seok, S., Il; Tio, N. Nanostructured TiO_2/$CH_3NH_3PbI_3$ Heterojunction Solar Cells Employing Spiro-OMeTAD/Co-Complex as Hole-Transporting Material. *J. Mater. Chem. A* **2013**, *1*, 11842.
17. Xiao, M.; Huang, F.; Huang, W.; Dkhissi, Y.; Zhu, Y.; Etheridge, J.; Gray-Weale, A.; Bach, U.; Cheng, Y. B.; Spiccia, L. A Fast Deposition-Crystallization Procedure for Highly Efficient Lead Iodide Perovskite Thin-Film Solar Cells. *Angew. Chem., Int. Ed.* **2014**, *126*, 10056–10061.
18. Malinkiewicz, O.; Roldán-Carmona, C.; Soriano, A.; Bandiello, E.; Camacho, L.; Nazeeruddin, M. K.; Bolink, H. J. Metal-Oxide-Free Methylammonium Lead Iodide Perovskite-Based Solar Cells: The Influence of Organic Charge Transport Layers. *Adv. Energy Mater.* **2014**, *4*, 1400345.
19. Im, J.-H.; Jang, I.-H.; Pellet, N.; Grätzel, M.; Park, N.-G. Growth of $CH_3NH_3PbI_3$ Cuboids with Controlled Size for High-Efficiency Perovskite Solar Cells. *Nat. Nanotechnol.* **2014**, *9*, 927–932.
20. Dar, M. I.; Ramos, F. J.; Xue, Z.; Liu, B.; Ahmad, S.; Shivashankar, S. A.; Nazeeruddin, M. K.; Grätzel, M. Photoanode Based on (001)-Oriented Anatase Nanoplatelets for Organic−Inorganic Lead Iodide Perovskite Solar Cell. *Chem. Mater.* **2014**, *26*, 4675–4678.
21. Lee, Y. H.; Stefik, M.; Heiniger, L.-P.; Gao, P.; Seok, S., Il Gratzel, M.; Nazeeruddin, M. K. *Power from the Sun: Perovskite Solar Cells*. In 2014 IEEE 40th Photovoltaic Specialist Conference (PVSC), Denver, CO, June 8−13, 2014; IEEE: New York, 2014; pp 0943−0948.
22. Leijtens, T.; Lauber, B.; Eperon, G. E.; Stranks, S. D.; Snaith, H. J. The Importance of Perovskite Pore Filling in Organometal Mixed Halide Sensitized TiO_2-Based Solar Cells. *J. Phys. Chem. Lett.* **2014**, *5*, 1096–1102.
23. Schiefer, S.; Zimmermann, B.; Glunz, S. W.; Würfel, U. Applicability of the Suns-V_{oc} Method on Organic Solar Cells. *IEEE J. Photovoltaics* **2014**, *4*, 271–277.
24. Tress, W.; Marinova, N.; Moehl, T.; Zakeeruddin, S. M.; Nazeeruddin, M. K.; Grätzel, M. Understanding the Rate-Dependent J−V Hysteresis, Slow Time Component, and Aging in $CH_3NH_3PbI_3$ Perovskite Solar Cells: The Role of a Compensated Electric Field. *Energy Environ. Sci.* **2015**, *8*, 995–1004.
25. Xing, G.; Mathews, N.; Lim, S. S.; Yantara, N.; Liu, X.; Sabba, D.; Grätzel, M.; Mhaisalkar, S.; Sum, T. C. Low-Temperature Solution-Processed Wavelength-Tunable Perovskites for Lasing. *Nat. Mater.* **2014**, *13*, 476–480.
26. Docampo, P.; Hey, A.; Guldin, S.; Gunning, R.; Steiner, U.; Snaith, H. J. Pore Filling of Spiro-OMeTAD in Solid-State Dye-Sensitized Solar Cells Determined *via* Optical Reflectometry. *Adv. Funct. Mater.* **2012**, *22*, 5010–5019.
27. Xing, G.; Mathews, N.; Sun, S.; Lim, S. S.; Lam, Y. M.; Grätzel, M.; Mhaisalkar, S.; Sum, T. C. Long-Range Balanced Electron- and Hole-Transport Lengths in Organic-Inorganic $CH_3NH_3PbI_3$. *Science* **2013**, *342*, 344–347.
28. Tress, W.; Marinova, N.; Inganäs, O.; Nazeeruddin, M. K.; Zakeeruddin, S. M.; Graetzel, M. Predicting the Open-Circuit Voltage of $CH_3NH_3PbI_3$ Perovskite Solar Cells Using Electroluminescence and Photovoltaic Quantum Efficiency Spectra: The Role of Radiative and Non-Radiative Recombination. *Adv. Energy Mater.* **2015**, *5*, DOI: 10.1002/aenm.201400812.
29. Reinhardt, J.; Grein, M.; Bühler, C.; Schubert, M.; Würfel, U. Identifying the Impact of Surface Recombination at Electrodes in Organic Solar Cells by Means of Electroluminescence and Modeling. *Adv. Energy Mater.* **2014**, *4*, 1–9.
30. Bi, D.; Yang, L.; Boschloo, G.; Hagfeldt, A.; Johansson, E. M. J. Effect of Different Hole Transport Materials on Recombination in $CH_3NH_3PbI_3$ Perovskite-Sensitized Mesoscopic Solar Cells. *J. Phys. Chem. Lett.* **2013**, *4*, 1532–1536.
31. Wehrenfennig, C.; Eperon, G. E.; Johnston, M. B.; Snaith, H. J.; Herz, L. M. High Charge Carrier Mobilities and Lifetimes in Organolead Trihalide Perovskites. *Adv. Mater.* **2014**, *26*, 1584–1589.
32. Stranks, S. D.; Burlakov, V. M.; Leijtens, T.; Ball, J. M.; Goriely, A.; Snaith, H. J. Recombination Kinetics in Organic-Inorganic Perovskites: Excitons, Free Charge, and Subgap States. *Phys. Rev. Appl.* **2014**, *2*, 034007.
33. Wetzelaer, G. A. H.; Kuik, M.; Lenes, M.; Blom, P. W. M. Origin of the Dark-Current Ideality Factor in Polymer:fullerene Bulk Heterojunction Solar Cells. *Appl. Phys. Lett.* **2011**, *99*, 153506.
34. Pysch, D.; Mette, A.; Glunz, S. W. A Review and Comparison of Different Methods to Determine the Series Resistance of Solar Cells. *Sol. Energy Mater. Sol. Cells* **2007**, *91*, 1698–1706.